Evolution of the surface passivation mechanism during the fabrication of ex-situ doped poly-Si(B)/SiOx passivating contacts for high-efficiency c-Si solar cells

Audrey Morisset, Raphaël Cabal, Valentin Giglia, Adrien Boulineau, Eric de Vito, Amal Chabli, Sébastien Dubois, J Alvarez, Jean-Paul Kleider

HAL Id: hal-03288976
https://hal.science/hal-03288976

Submitted on 5 Aug 2021

Evolution of the surface passivation mechanism during the fabrication of ex-situ doped poly-Si(B)/SiOₓ passivating contacts for high-efficiency c-Si solar cells

Audrey Morisset[a,c,d,e,#,*], Raphaël Cabal[a,*], Valentin Giglia[a], Adrien Boulineau[b], Eric De Vito[b], Amal Chabli[a], Sébastien Dubois[a], Jose Alvarez[c,d,e] and Jean-Paul Kleider[c,d,e].

a. Univ. Grenoble Alpes, CEA, LITEN, DTS, INES, F-73375, Le Bourget Du Lac, France.

b. Univ. Grenoble ALPES, CEA, LITEN, DTNM, 17 rue des Martyrs, F-38000 Grenoble, France.

c. Université Paris-Saclay, CentraleSupélec, CNRS, Laboratoire de Génie Electrique et Electronique de Paris, F-91192, Gif-sur-Yvette, France.

d. Sorbonne Université, CNRS, Laboratoire de Génie Electrique et Electronique de Paris, F-75252, Paris, France.

e. Institut Photovoltaïque d'Ile-de-France (IPVF), 30 RD 128, F-91120, Palaiseau, France.

[#]Present address: *Ecole Polytechnique Fédérale de Lausanne (EPFL), Institute of Microengineering (IMT), Photovoltaics and Thin Film Electronics Laboratory, Rue de La Maladière 71b, 2002, Neuchâtel, Switzerland.*

*Corresponding authors: audrey.morisset@epfl.ch, raphael.cabal@cea.fr

Abstract

Passivating the contacts of crystalline silicon (c-Si) solar cells (SC) with a poly-crystalline silicon (poly-Si) layer on top of a thin silicon oxide (SiOₓ) is currently sparking interest for reducing carrier recombination at the interface between the metal electrode and the c-Si substrate. However, due to the interrelation between different mechanisms at play, a comprehensive understanding of the surface passivation provided by the poly-Si/SiOₓ contact in the final SC has not been achieved yet. In the present work, we report on an original ex-situ doping process of the poly-Si layer through the deposition of a B-rich dielectric layer followed by an annealing step to diffuse B dopants in the layer. We propose an in-depth investigation of the passivation scheme of the resulting B-doped poly-Si/SiOₓ contact by first comparing the surface passivation provided by ex-situ doped and intrinsic poly-Si/SiOₓ contacts at different steps of the fabrication process. The excellent surface passivation properties obtained with the ex-situ doped poly-Si(B) contact (iV_{oc} = 733 mV and J_0 = 6.1 fA cm^{-2}) attests to the good quality of this contact. We then propose further STEM, ECV and ToF-SIMS characterizations to assess: i) the evolution of the microstructure and

B-doping profile through ex-situ doping and ii) the diffusion profile of hydrogen in the poly-Si contact. Our results show a gradual filling of the poly-Si layer with active B dopants with increasing annealing temperature (T_a), which strengthens the field-effect passivation and enables an iV_{oc} increase after annealing up to 800 °C. We also observe a diffusion of O from the SiON:B doping layer to the interfacial SiO_x layer during annealing, that likely enhances the passivation stability of our ex-situ doped poly-Si contact with increasing T_a. Finally, we conclude that the mechanism dominating the surface passivation changes during the fabrication process of the poly-Si/SiO_x contact from field-effect passivation after annealing (performed for B-diffusion in the contact) to chemical passivation after following hydrogenation of the samples (performed by depositing a H-rich silicon nitride layer).

Keywords

Crystalline silicon, solar cells, passivating contacts, Poly-silicon, PECVD

1. Introduction

In the currently industrialized p-type crystalline-silicon (c-Si) solar cells (SC), the charge collection from the c-Si substrate to the metal electrode occurs by direct contacts between the c-Si and the metal. This is performed either through a full area contact in the Aluminium-Back Surface Field (Al-BSF) structure or through localized contacts in the Passivated Emitter and Rear Cell (PERC) one [1]. However, these direct metal/c-Si interfaces are highly defective and remain one of the main limitations of the performances of c-Si SC, even when localized like in the PERC structure [2]. In this context, the concept of full-area passivating contacts emerged with the aim of fully passivating the defective metal/c-Si interfaces while ensuring an effective transport of charge carrier towards the metal electrode [1]. One promising full area passivating contact consists of a stack of a highly-doped polycrystalline silicon (poly-Si) layer on top of a thin silicon oxide (SiO_x) layer. This poly-Si/SiO_x contact has demonstrated excellent surface passivation properties and recently enabled photovoltaic conversion efficiencies close to 26 % when integrated in small-area n-type c-Si SC (2x2 cm^2) [3,4]. More recently, efficiencies up to 24.58 % were also demonstrated with an electron-selective poly-Si contact integrated at the rear side of large-area n-type c-Si SC with screen-printed metal electrodes [5,6].

The fabrication process of the poly-Si/SiO$_x$ contact relies on the three following steps: i) the growth of a thin SiO$_x$ layer at the c-Si surface, ii) the deposition of a Si-based layer (generally doped with B or P either during deposition or right after) and iii) an annealing step at high-temperature typically performed in the range 700-1000 °C. This last step targets to crystallizing the Si layer (then referred to as 'poly-Si') as well as activating and/or diffusing dopants. Among the possible techniques to deposit the Si-based layer, the Plasma-Enhanced Chemical Vapor Deposition (PECVD) is particularly interesting as it enables for: i) single-side deposition and ii) tuning of the layer's properties (e.g. mechanical or optical) through doping with additional elements (like C or O) [7,8]. However, a major drawback of this technique is the high amount of hydrogen incorporated in the Si-based layer, responsible for so-called 'blistering' of the layer if the deposition conditions are not carefully optimized [8–11].

When successfully fabricated, the poly-Si/SiO$_x$ contact allows for low recombination current densities (J$_0$ = 1-10 fA cm^{-2}) at the c-Si surface, resulting in an increase of the open-circuit voltage (V$_{oc}$ = 715-727 mV) of the final SC [3–5,12]. These excellent surface passivation properties likely rely on the combination of [13,14]:

1. The thin SiO$_x$ layer along the interface providing chemical passivation of the c-Si surface;

2. The high-doping density in the poly-Si layer featuring a sharp diffusion profile at the c-Si surface providing field-effect passivation;

3. The diffusion of H in the structure, performed through an additional hydrogenation step, providing further chemical passivation of the interface.

The robustness of the poly-Si layer against the subsequent implementation of a metal electrode is also an important requirement to preserve a good surface passivation of the c-Si in the final SC [15]. The passivation efficiency of the features described above (1-3) strongly depends on the fabrication process of the poly-Si/SiO$_x$ contact [8,16,17]. This implies convoluted interdependences between these different passivation features, which has, for now, prevented the clear discrimination of their respective contributions to the global surface passivation of the c-Si in the final SC.

In a previous study, we reported on an original ex-situ doping process of the poly-Si/SiO$_x$ contacts [18]. This process relies on the deposition of an intrinsic Si layer by PECVD, which is ex-situ doped through the deposition of a B-rich dielectric layer followed by an annealing step at high temperature (700-850 °C). In the present work, we report on an in-depth study

of the passivation scheme of this ex-situ doped poly-Si contact. We first compare the surface passivation properties of intrinsic and ex-situ doped poly-Si/SiO$_x$ contacts at different steps of the fabrication process. To get deeper insights, we then investigate: i) the evolution of the microstructure of the as-deposited Si layer and of the thin SiO$_x$ layer through ex-situ doping, ii) the resulting B doping profile as a function of the annealing temperature for poly-Si crystallization and dopant diffusion, and iii) the H concentration profiles in intrinsic and doped poly-Si/SiO$_x$ contacts after hydrogenation.

2. Material and methods

2.1. Sample preparation

All the c-Si substrates used in this study were n-type (100)-oriented c-Si wafers from Czochralski (Cz) grown silicon ingots. For the passivation study, we used 180 µm-thick KOH-polished wafers with a size of 156x156 mm^2 and a resistivity in the range 3-6 Ω.cm. For physical and chemical characterizations that require flat interfaces, we used 275 µm-thick 4-inch wafers with mirror-polished surfaces and a resistivity in the range 2-3 Ω.cm. In the following, we refer to these two kinds of wafers as 'KOH-polished substrates' and 'M-polished substrates', respectively.

A schematic of the fabrication process of the ex-situ B-doped poly-Si/SiO$_x$ contact is presented in **Figure 1**. First, the wafers were cleaned through a standard RCA cleaning sequence performed in an automated wet bench 'V3 system' from Akrion. A 2 min-long rinsing step in ozonized deionized water was added at the end of the sequence to grow a thin SiO$_x$ layer (1.4±0.1 nm) at the surface of the wafers. Then, a 25 nm-thick intrinsic Si layer (without intentional doping) was deposited by PECVD using SiH$_4$ and H$_2$ as precursor gases (with a ratio H$_2$/SiH$_4$ = 40) at a deposition temperature of 300 °C. In the following, this layer is denoted 'as-dep Si(i) layer'. For ex-situ doping, a B-rich silicon oxynitride layer (SiO$_x$N$_y$:B denoted 'SiON:B') was then deposited by PECVD on top of the as-dep Si(i) layer using a mixture of SiH$_4$, N$_2$O and H$_2$ diluted B$_2$H$_6$ and a deposition temperature of 300 °C . A subsequent annealing step was performed in a tube furnace under argon atmosphere in the temperature range 700-850 °C to ensure the diffusion of B atoms in the as-dep Si(i) layer. The samples were loaded in the tube furnace at a temperature of 400 °C and a ramp rate of ~10 °C/min was then applied to reach the desired annealing temperature (T$_a$) for a 30 min

plateau. A ramp rate down of 10 °C/min was applied to unload the samples at 700 °C. In the following, the resulting B-doped Si layer after annealing is referred to as 'poly-Si(B)'.

Intrinsic poly-Si/SiO$_x$ passivating contacts were also fabricated using the same process but omitting the deposition of the SiON:B doping layer (**Figure 1**). In the following, the intrinsic layer after annealing is referred to as 'poly-Si(i)' in order to differentiate it from the intrinsic layer after deposition (denoted 'as-dep Si(i)').

A hydrogenation step was then performed on both B-doped and intrinsic poly-Si/SiO$_x$ contacts by PECVD of a H-rich silicon nitride (SiN:H) layer (deposited directly on top of the SiON:B layer in the case of B-doped contacts as illustrated in **Figure 1**), followed by a firing step in a belt furnace with a peak temperature of approximately 880 °C.
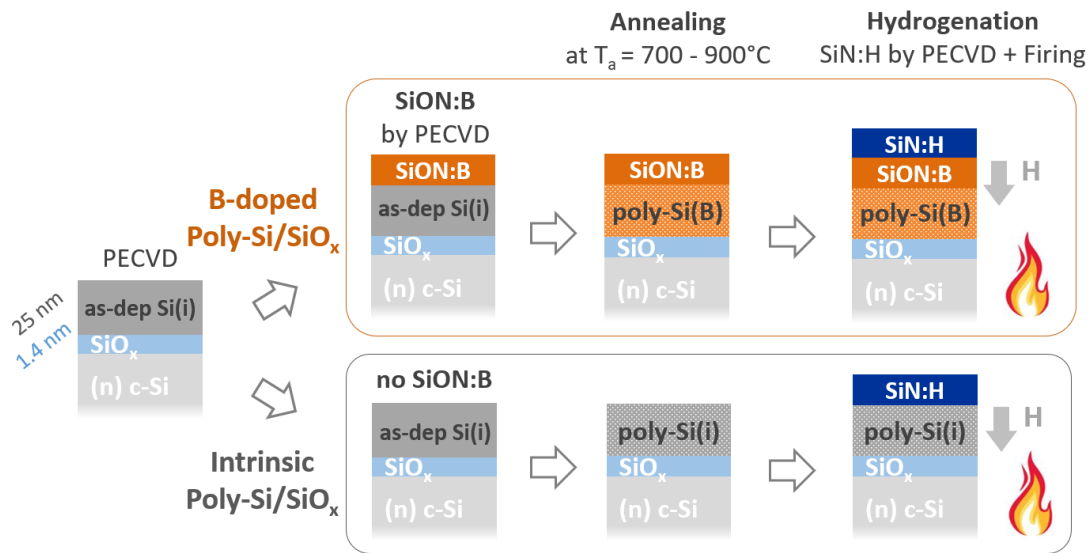
Figure 1. Schematic of the fabrication processes of B-doped and intrinsic poly-Si/SiO$_x$ contacts.

2.2. Characterization

Spectroscopic ellipsometry (SE) measurements were performed on M-polished samples to evaluate the thicknesses of the as-dep Si(i), poly-Si(i) and poly-Si(B) layers. The optical functions of the layers were recorded from 1.5 to 5.2 eV using a UVISEL tool from Horiba Jobin Yvon with a Xenon lamp as the excitation source. The software Delta Psi 2 associated to this tool was used to fit the resulting data considering layers consisting of crystalline clusters in an amorphous matrix (model adapted from refs. [19,20]).

The Scanning Transmission Electron Microscopy (STEM) was used to observe the microstructure of as-dep Si(i), poly-Si(i) and poly-Si(B) layers of M-polished samples. The STEM samples were prepared using a Focused-Ion Beam (FIB) to obtain 80 nm-thick and

10 µm-large lamellas. HRSTEM images were recorded using a Titan Themis microscope (from FEI) operated at 200 keV. The Electron Energy Loss Spectroscopy (EELS) mode of this microscope was used for further chemical analyses of the samples, more specifically to map the oxygen distribution in the samples observed by STEM. EELS elemental maps were calculated from EELS spectra acquired using a GIF Quantum spectrometer.

Electrochemical Capacitance-Voltage (ECV) measurements were carried out to estimate the majority carrier concentration profile in poly-Si(B) layers, using an ECV CVP21 tool from WEP with a 0.1 mol/L NH_4F solution as etchant. In the following, the majority carrier concentration measured by ECV is approximated as the active B concentration. Hall effect measurements were performed using a HMS-5500 tool from Ecopia to assess the electrical properties (conductivity, Hall mobility and charge carrier concentration) of the poly-Si(B) layer on laser cut 2×2 cm^2 pieces of the samples.

Time-of-Flight Secondary Ion Mass Spectroscopy (ToF-SIMS) measurements were performed with a TOF.SIMS.5 equipment from IONTOF to measure the total B concentration profile in the poly-Si(B) layer as well as H and O concentration profiles in both poly-Si(B) and poly-Si(i) contacts. Bi^+ ions with an energy of 25 keV were used as the primary ion source. Cs^+ ions with an energy of 1 keV were used as the sputtering ion source to measure in-depth profiles. The analysed surface areas (~ 80x80 µm^2) were centred within the sputtered surface area (~ 300x300 µm^2). Since the samples analysed by ToF-SIMS consisted of stacks of different materials, the ToF-SIMS sputtering rate was expected to differ from one layer to another, thus, the ToF-SIMS sputtering time was not converted into thickness. The atomic concentration was calculated by using calibration data obtained from reference samples.

The photo-conductance decay (PCD) technique was applied on symmetrical samples made from KOH-polished substrates using a WCT-120 tool from Sinton Instruments to assess the implied open circuit voltage (iV$_{oc}$) at different steps of the fabrication process. In addition to iV$_{oc}$, the emitter recombination current density (J$_0$) associated to a single surface was also extracted according to the method of Kane and Swanson [21].

Symmetrical samples made from KOH-polished substrates were used for the PCD measurements while one-sided samples made from M-polished substrates were used for SE, STEM, ECV, Hall effect and ToF-SIMS characterizations.

3. Results & discussion

3.1. Surface passivation properties of poly-Si(i) and poly-Si(B) contacts

The development of the ex-situ doping process allowed for the fabrication of intrinsic poly-Si/SiO$_x$ contacts by omitting the SiON:B deposition before the annealing step. In this first part, we compare the surface passivation of ex-situ doped and intrinsic poly-Si/SiO$_x$ contacts in order to better understand the respective contributions of the chemical passivation and field-effect passivation to the overall surface passivation provided by the poly-Si contact. The ex-situ doping method used in this work relies on thermal diffusion, which is less likely to induce damages of the poly-Si layer than ion implantation for example [22]. Therefore, in the following, we assume that the only significant difference between the poly-Si(i) and poly-Si(B) contacts is the presence of the SiON:B layer on top of the latter, applied for diffusing B dopants in the poly-Si layer during annealing. We note that the presence of this SiON:B layer could also induce the diffusion of other elements (e.g. O) in the doped structures.

Symmetrical samples were prepared with either B-doped or intrinsic poly-Si/SiO$_x$ contacts on both sides of KOH-polished substrates. Samples were annealed at a temperature (T$_a$) in the range of 700-850 °C. The passivation level provided by poly-Si(i) and poly-Si(B) contacts was evaluated (in terms of iV$_{oc}$ and J$_0$) as a function of T$_a$ after the different steps of the process illustrated in **Figure 1**, namely, after annealing, after SiN:H deposition and after firing. The results are shown in **Figure 2**.
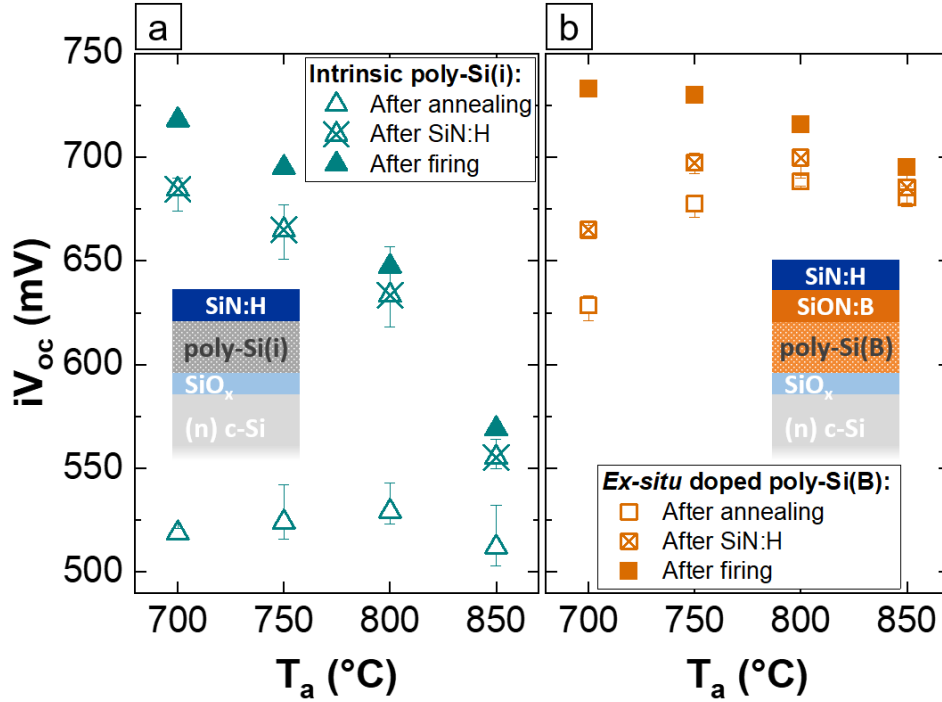
Figure 2. iV_{oc} measured by PCD on symmetrical samples (with poly-Si/SiO$_x$ contacts fabricated on both sides of the c-Si substrate) as a function of the annealing temperature T_a. The measurement was performed on samples featuring intrinsic poly-Si layers (poly-Si(i)) (a) and B-doped poly-Si layers (poly-Si(B)) (b) after annealing, after SiN:H deposition and after firing of the all stack. We note that measurements after SiN:H and after firing were performed with the SiN:H capping layer (see inset schematics).

After annealing (shown by the open symbols in **Figure 2**), one can observe that:

- The poly-Si(i) contact showed poor iV_{oc} values (< 530 mV) in the investigated T_a range whereas poly-Si(B) demonstrated decent iV_{oc} values (up to 688 mV for T_a = 800 °C, corresponding to J_0 = 44.8 fA·cm^2);

- For T_a from 700 °C to 800 °C, the poly-Si(B) contact demonstrated an increase of iV_{oc} from 628 mV to 688 mV followed by a decrease for T_a = 850 °C to 680 mV. For the poly-Si(i) contact, iV_{oc} fluctuated around 525 mV on the investigated T_a range, with only a slight decrease of the mean iV_{oc} value observed for T_a = 850 °C.

The low iV_{oc} values obtained with the poly-Si(i) contact evidenced a poor chemical passivation provided by the SiO$_x$ layer alone at this stage of process, as similarly reported in ref. [14]. It thus emphasized the importance of the field-effect passivation related to the high B-doping of the poly-Si layer to obtain iV_{oc} values greater than 625 mV after annealing.

Regarding the iV_{oc} versus T_a trend after annealing, one can note that:

- For the poly-Si(i) contact the surface passivation is only provided by the thin SiO_x layer. Thus, the slight decrease of iV_{oc} observed for $T_a > 800$ °C could be attributed to a degradation of the thin SiO_x layer (homogeneity and/or bonding structure) along the interface [16,23];

- For the poly-Si(B) contact, the field-effect passivation related to the high B-doping has to be taken into account. The increase of iV_{oc} from $T_a = 700$ °C to 800 °C could result from an increased field-effect passivation due to the gradual diffusion of dopants in the poly-Si layer. The decrease of iV_{oc} at high T_a (here for $T_a > 800$ °C) is typical for doped poly-Si contacts and is generally attributed to the afore-mentioned degradation of the thin SiO_x layer as well as a too deep diffusion of dopant in the c-Si substrate, which could involve significant Auger recombination [24,25].

The contribution of Auger recombination in the doped c-Si(p^+) region ($J_{0,Auger}$) to the total recombination current density (J_0) was evaluated using the software Edna 2, with the active B doping profile in the c-Si measured by ECV as an input (see **Figure 6**) [26–28]. This analysis was performed for samples exhibiting a significant B diffusion-tail in the c-Si, namely for $T_a = 800$ °C and 850 °C. As illustrated in **Table 1**, the contribution of $J_{0,Auger}$ was found to represent 9.6% and 13.4% of the total J_0 for $T_a = 800$°C and 850°C, respectively. This indicates that, while being significant, the Auger recombination can only partially account for the loss of passivation observed with increasing T_a from 800 °C to 850 °C, and that some other interface mechanisms (e.g. SiO_x degradation) may also take place with such a T_a increase.

Table 1. Total recombination current density (J_0) and contribution of Auger recombination in the doped c-Si(p^+) region ($J_{0,Auger}$) (obtained by PCD measurements and calculated through Edna 2, respectively) at different annealing temperature (T_a). We note that both J_0 and $J_{0,Auger}$ are mirroring recombination at a single surface of the associated symmetrical samples.

T_a (°C)	J_0 (fA·cm^2)	$J_{0,Auger}$ (fA·cm^2)
800	44.8	4.3
850	52.4	7.0

After SiN:H deposition (shown by the crossed-symbols in **Figure 2**), one can observe for both poly-Si(i) and poly-Si(B) contacts:

- An increase of iV_{oc} in the whole investigated T_a range;
- A decreasing gain in iV_{oc} with increasing T_a.

The deposition of a SiN:H layers is known to provide both field-effect passivation due to positive fixed charges and chemical passivation due to H-diffusion in the sample [29]. However, for both poly-Si(i) and poly-Si(B) contacts, the surface passivation properties (iV_{oc} and J_0) were found to be stable after etching of the SiN:H layer by dipping the samples for a few seconds in a concentrated HF solution. Therefore, the iV_{oc} increase observed here is likely linked to the diffusion of H in the samples. Although the poly-Si(i) contact showed a greater iV_{oc} gain after SiN:H deposition (up to 160 mV for T_a = 700 °C), the poly-Si(B) contact showed a better stability of surface passivation at high $T_a \geq 750$ °C with iV_{oc} greater than 675 mV (associated to J_0 values lower than 45 fA·cm^2). This latter observation probably results from the additional field-effect passivation related to the high B-doping of the poly-Si layer.

Regarding the second observation, as already mentioned, the bonding structure in the SiO$_x$ layer and/or at the SiO$_x$/c-Si interface is likely to change during annealing at high T_a, which could change the ability of H to bond at the interface and thus decrease the efficiency of the hydrogenation process to cure interface defects and enhance the surface passivation. The diffusion of H in poly-Si(i) and poly-Si(B) contacts will be further investigated and discussed in **section 3.2.3**.

Finally, the firing step performed after the SiN:H deposition allowed for further improvement of the surface passivation as observed from the increase of iV_{oc} for both intrinsic and doped contacts, which probably results from the further diffusion of H in the structures. After firing (shown by solid symbols in **Figure 2**), one can note similar trends to those after SiN:H deposition:

- An overall higher surface passivation and better stability with increasing annealing temperature provided by poly-Si(B) compared to poly-Si(i), likely resulting from the additional B-doping related field-effect;

- A better iV_{oc} gain for samples previously annealed at $T_a \leq 750\,°C$ compared to samples annealed at $T_a \geq 800\,°C$ for both intrinsic and doped contacts.

After firing, the only noticeable difference was a change of the iV_{oc} versus T_a trend for the poly-Si(B) contact. In fact, the best iV_{oc} value of 733 mV (corresponding to $J_0 = 6.1\ fA·cm^2$) was obtained for $T_a = 700\,°C$ and iV_{oc} then steadily decreased with increasing T_a, whereas before firing, the highest iV_{oc} was obtained for $T_a = 800\,°C$.

In conclusion, the comparison of iV_{oc} measured on samples featuring poly-Si(i) and poly-Si(B) contacts enabled to observe:

- After annealing, a negligible surface passivation provided by the SiO_x layer alone, thus, the importance of the poly-Si high-doping providing additional field-effect passivation at this stage of the process;
- After SiN:H deposition and firing, an important gain of iV_{oc} for both intrinsic and doped contacts, likely resulting from H diffusing toward the SiO_x interface. This iV_{oc} gain rapidly decreased with increasing T_a, which could result from changes of the SiO_x/c-Si interface structure with increasing T_a, decreasing the efficiency of the hydrogenation of the interface.

In the following part, additional characterizations are performed to further investigate these results, with a particular focus on the impact of the SiON:B doping layer on the surface passivation properties of the ex-situ doped poly-Si contact.

3.2. Further investigations of the impact of ex-situ doping on surface passivation

3.2.1. Evolution of the layer microstructure during ex-situ doping

Firstly, we investigated by STEM the evolution of the microstructure of the as-dep Si(i) layer through ex-situ doping. The analyses were performed on samples with the respective as-dep Si(i), poly-Si(i) and poly-Si(B) layer on one side of M-polished substrates (denoted sample 1, 2 and 3, respectively). The annealing step involved in the process of poly-Si(i) and poly-Si(B) layers was performed at $T_a = 800\,°C$ (see **Figure 1**).

Figure 3 shows the results of the STEM and EELS analyses of the three samples. After deposition, the as-dep Si(i) layer appeared nanocrystalline with randomly oriented

crystalline domains of a few nanometres (Sample 1, **Figure 3a**). We note that the high gas flow ratio between H_2 and SiH_4 applied during the PECVD step (H_2/SiH_4 = 40) likely explains the deposition of an already nanocrystalline Si layer [30]. After annealing at 800 °C, the poly-Si(i) layer still appeared nanocrystalline with a very similar microstructure to the as-dep Si(i) layer i.e. randomly oriented crystalline domains in the nanometric range (**Figure 3b**). These observations indicate that the microstructure of the intrinsic Si layer was set from the deposition step and remained stable through a subsequent annealing step. The STEM analysis of sample 3 (**Figure 3c**) showed that the poly-Si(B) layer is also nanocrystalline and seems to feature slightly bigger crystalline domains compared to the as-dep Si(i) and poly-Si(i) layers. Some crystalline domains even appear columnar along the 25 nm-thick layer, one of which is emphasized with a circle inserted in **Figure 3c**.
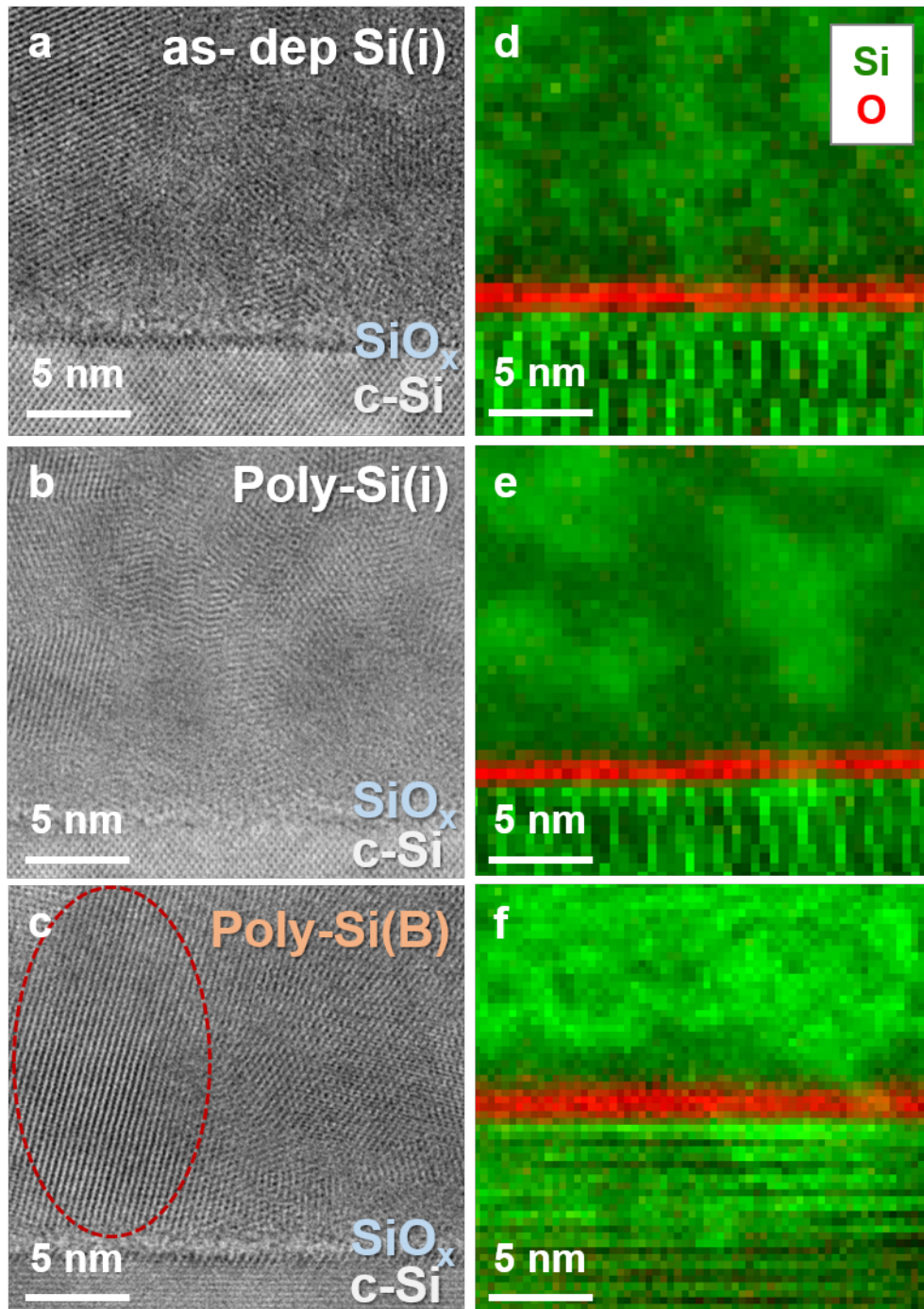
Figure 3. HR-STEM images of the as-dep Si(i) layer after deposition (a), the poly-Si(i) layer after deposition and annealing at $T_a = 800\,°C$ (b) and the poly-Si(B) layer after deposition of the SiON:B doping layer on top of the as-dep Si(i) layer and annealing at $T_a = 800\,°C$ (c). The respective EELS elemental maps of these samples (d) (e) and (f) are depicted beside the STEM images (we note that STEM images and EELS maps were not measured exactly in the same areas).

The imaginary part of the dielectric function (ε_i) measured as a function of the photon energy (E_{ph}) by SE can also provide information about the microstructure of the layers at a

macroscopic scale, as a complement to STEM which is a very local technique. For crystalline silicon the ε_i versus E_{ph} curve exhibits sharp peaks at 3.4 and 4.2 eV, while in amorphous silicon a single broad peak is observed at 3.6-3.8 eV [19,20]. The ε_i versus E_{ph} curves associated to the as-dep Si(i), poly-Si(i) and poly-Si(B) are shown in **Figure 4**. Although the curves are not identical, they all exhibit a smooth shape with a kind of plateau between two peaks centred around 3.3 and 4.2 eV, which is typical of a Si layer with nanometric grains and featuring some surface porosity [19]. This observation is in good agreement with the STEM results although it suggests that, at a larger scale, the microstructure of the different layers appears quite similar.
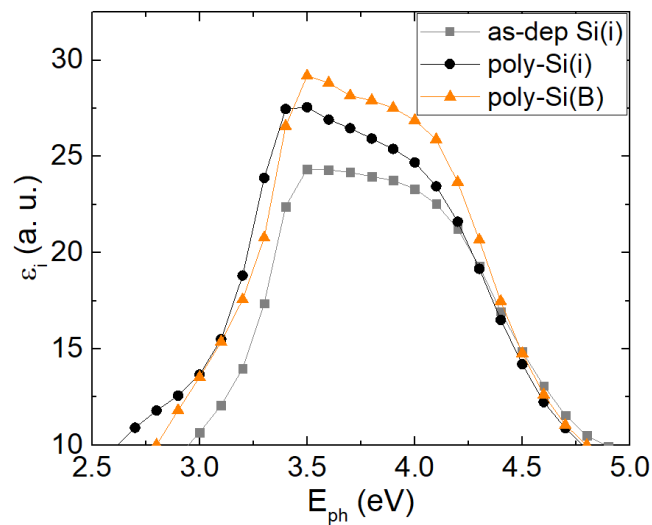
Figure 4. Imaginary part of the pseudo-dielectric function (ε_i) versus photon energy (E_{ph}) obtained by spectroscopic ellipsometry (SE) measurement of the as-dep Si(i) layer after deposition, the poly-Si(i) layer after deposition and annealing at T_a = 800 °C and the poly-Si(B) layer after deposition of the SiON:B doping layer on top of the as-dep Si(i) layer and annealing at T_a = 800 °C.

The EELS analyses (coupled to STEM) enabled the mapping of the O distribution in the poly-Si/SiO$_x$ contact. One can observe a peak of O distribution along the interface between the as-dep Si/poly-Si layers and the c-Si substrate, corresponding to the thin SiO$_x$ layer (**Figure 3d, e & f**). To better compare the EELS results obtained on the different samples, the average O distribution profiles were extracted along an axis perpendicular to the samples surface and were superimposed on the same graph (**Figure 5**). Since the EELS signal depends on the counting time and the lamella thickness, the intensities of the O peaks obtained were not quantitatively comparable and were thus normalized to their maximum value. This representation enables to observe a larger full-width at half-maximum of the peak

associated to sample 3 (featuring the poly-Si(B) layer) compared to the two other peaks. This indicates a broader O distribution at the SiO$_x$ interface of sample 3 i.e. after ex-situ B-doping. Moreover, for this same sample, one can observe a significant O distribution in the c-Si substrate. These two observations likely arise from the presence of the SiON:B doping layer that allows for O atoms to diffuse towards the interfacial SiO$_x$ layer and in the c-Si substrate during annealing.
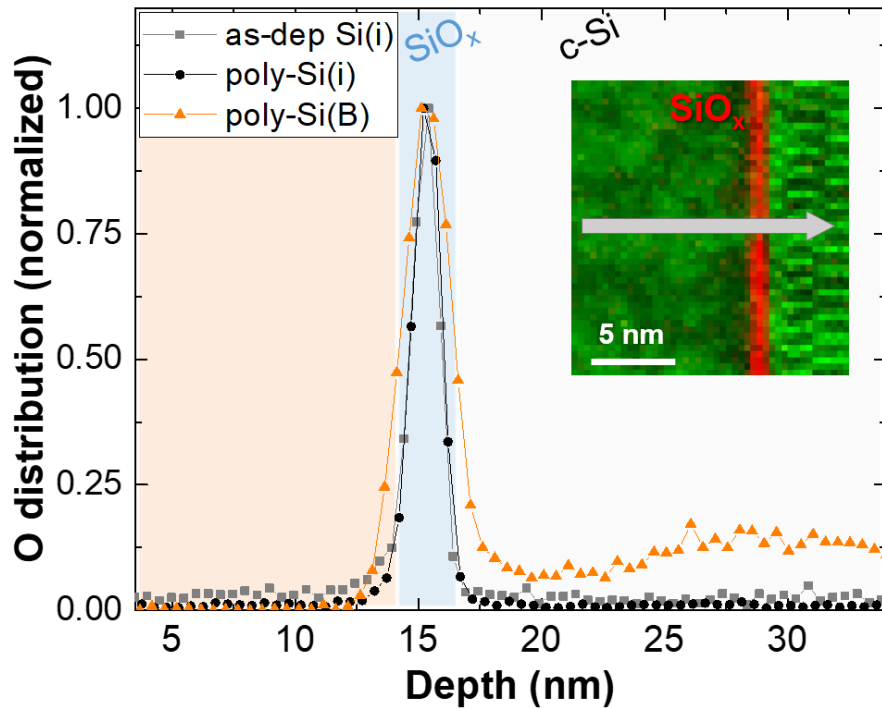
Figure 5. O distribution profiles assessed by EELS after deposition of the intrinsic Si layer (as-dep Si(i)), after annealing at T$_a$ = 800 °C (poly-Si(i)) and after SiON:B deposition plus annealing at T$_a$ = 800 °C (poly-Si(B)). Each profile is an average of the profiles extracted from the respective EELS image along the direction perpendicular to the sample's surface (see arrow in the inset). The intensity of the O peaks was normalized to their maximum value.

To sum up, the STEM and SE analyses presented in this section showed a similar microstructure for the as-dep Si(i), poly-Si(i) and poly-Si(B) layers (after deposition, after annealing and after ex-situ doping, respectively), emphasizing the stability of the layer's microstructure upon a simple annealing step at high temperature and upon ex-situ doping. For the ex-situ doped poly-Si(B) sample, a broader O distribution was observed in the region of the interfacial SiO$_x$ layer, which likely results from the diffusion of O atoms from the SiON:B doping layer to the interfacial SiO$_x$ layer during annealing. Such an additional source

15

of O during annealing could partly explain the better stability of surface passivation with increasing T_a demonstrated by the doped poly-Si contact compared to its intrinsic counterpart (see **Figure 2**) [31].

3.2.2. Variation of the doping profile with increasing annealing temperature

The doping profile in the poly-Si layer and at the surface of the c-Si substrate is known to play a role in the final surface passivation properties of the poly-Si/SiO$_x$ contact [17,32]. Thus, in this paragraph, we focus on the variation of the B-doping profile of the ex-situ doped poly-Si/SiO$_x$ contact with increasing annealing temperature T_a.

For this study, samples with the ex-situ doped poly-Si/SiO$_x$ contact on one side of M-polished wafers were fabricated with the annealing temperature T_a varying in the range 700-850 °C. The active B concentration profiles were measured by ECV after etching the SiON:B doping layer by dipping the samples in a concentrated HF solution. The total B concentration profiles were measured by ToF-SIMS without previous etching of the SiON:B layer.

Figure 6 shows the resulting active and total B concentration profiles represented with symbols and dotted lines, respectively. The ToF-SIMS and ECV profiles were compared by aligning the ToF-SIMS sputtering time corresponding to the poly-Si top surface (~ 460 s) with the first point measured by ECV (etching depth of 0 nm). By doing so, we observed a good match between the edge of total and active B profiles (especially for $T_a \geq 800$ °C), exhibiting that the c-Si substrate was reached (for a sputtering time of 560 s and an etching depth of 22 nm, respectively) and therefore indicating the approximate position of the thin SiO$_x$ layer.
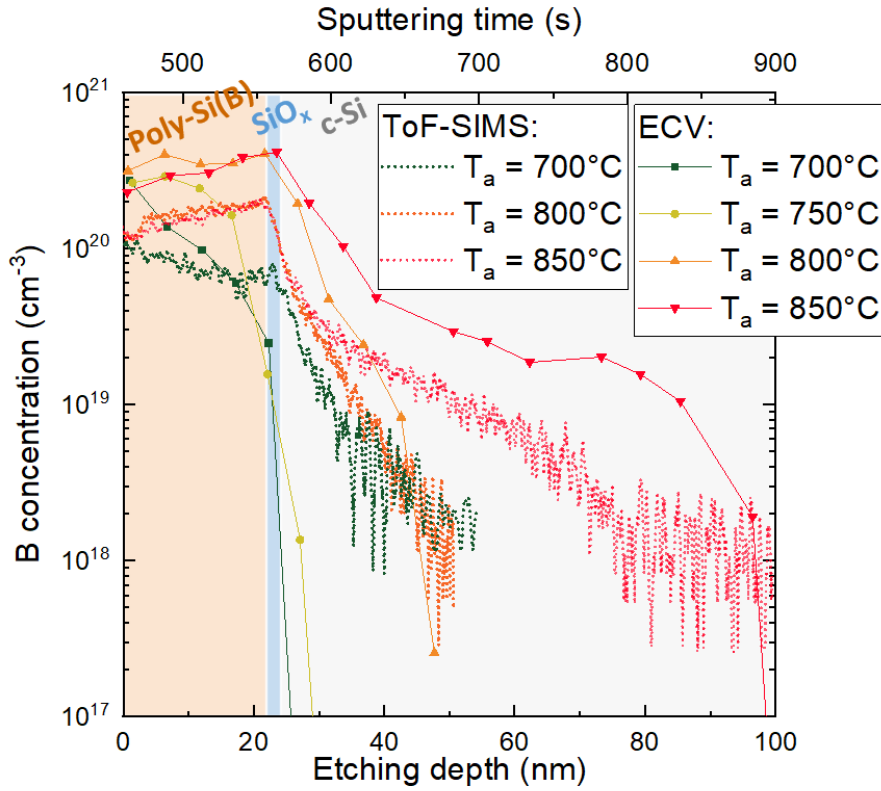
Figure 6. Active and total B concentration profiles measured by ECV and ToF-SIMS, respectively, on ex-situ doped poly-Si/SiO$_x$ contacts after annealing at various annealing temperatures T$_a$. The etching depth on the bottom x-axis and the sputtering time on the top x-axis refer to the ECV and ToF-SIMS measurements, respectively. The SiON:B doping layer was not etched before ToF-SIMS analysis but is not represented in this graph.

Focusing on the active B profiles, the following observations can be underlined:

- For T$_a$ = 700 °C and 750 °C, the profiles showed a gradient of the active B concentration in the poly-Si(B) layer from 3×10^{20} cm^{-3} to 2×10^{19} cm^{-3};

- For T$_a$ = 800 °C and 850 °C, the profiles featured a doping plateau around 2×10^{20} cm^{-3} in the poly-Si(B) layer coupled with a shallow diffusion of active B dopants in the c-Si substrate up to 25 nm and 80 nm, respectively.

These observations emphasize the gradual filling of the poly-Si(B) layer with active B dopants with increasing T$_a$, which is consistent with the diffusion-based doping process applied here. The gradual filling of the poly-Si(B) layer with active dopants and the further thin B diffusion in the c-Si for T$_a$ = 800 °C likely resulted in a strengthened field-effect at the c-Si surface, which could explain the increase of iV$_{oc}$ observed after annealing from T$_a$ = 700 °C to T$_a$ = 800 °C (see **Figure 2**).

Comparing the total and active B profiles, one can observe an overall good agreement of the profiles' shapes at each T_a. The noticeable differences between total and active B profiles are:

- A slightly higher active B concentration in the poly-Si(B) layer for the whole investigated T_a range as well as in the c-Si for T_a = 800 °C and 850 °C;

- For T_a = 700 °C, a B diffusion tail of approximately 25 nm measured by ToF-SIMS in the c-Si, whereas no active B diffusion was revealed by ECV.

The active B concentration measured by ECV is likely overestimated since it could not be higher than the total B concentration measured by ToF-SIMS. The active B concentration was also evaluated by Hall effect measurements on similar samples after annealing at T_a = 700 °C and 750 °C (to ensure no B diffusion in the c-Si substrate) and was found to be ten times lower (1.2×10^{19} cm^{-3} and 1.5×10^{19} cm^{-3}, respectively) than the one assessed by ECV at the poly-Si surface. We note that the active B concentration evaluated by Hall effect represents a mean value of the gradient doping profile observed in the poly-Si layer for T_a = 700 °C and 750 °C, which could explain the order of magnitude difference with the ECV surface concentration. The overestimation of the active B concentration measured by ECV in the c-Si could result from an increasing underestimation of the contact area between the electrolyte and the sample's surface with increasing etching depth [33]. Regarding the second observation, the evaluation of steep doping gradient by ToF-SIMS can be challenging due to some measurement artefacts (e.g. knock-on effects), which could explain the deeper B diffusion length observed by ToF-SIMS as compared to ECV for T_a = 700 °C.

Overall, these results emphasize the suitability of the ex-situ doping process to reach active B doping concentration of at least 1×10^{19} cm^{-3} in the poly-Si layer and thus ensure an effective field-effect passivation at the c-Si surface. Compared to the conventional in-situ doping of PECVD poly-Si layers, the ex-situ doping process applied here offers the advantage of no addition of a doping precursor (e.g. B_2H_6) during deposition of the Si layer, which is known to affect the layer's properties [8,11]. This results in: i) an easier optimization of the deposition conditions of the Si layer and ii) a better control of the doping profile that is then decoupled from the Si layer deposition step. Moreover, compared to other ex-situ doping processes (e.g. based on BBr_3 diffusion or ion implantation), the one proposed here involves only one additional process step compared to in-situ doping, namely the deposition of the

SiON:B doping layer by PECVD, which can be used as an anti-reflective coating and thus does not require subsequent etching [34]. We also note that the as-dep Si(i)/SiON:B stack could in principle be deposited through a unique PECVD step, which could make this ex-situ doping process comparable to in-situ doping in terms of number of process steps.

3.2.3. H distribution in poly-Si(i) and poly-Si(B) contacts

In this last section, we detail our investigations of the H concentration profile in poly-Si(i) and poly-Si(B) contacts. H and O concentration profiles were measured by ToF-SIMS after SiN:H deposition on poly-Si(i) and SiON:B capped poly-Si(B) layers annealed at the lowest (700 °C) and highest (850 °C) T_a over the investigated range. The resulting profiles are shown in **Figure 7**. For the sake of simplicity, the H and O concentration profiles were represented in the region of interest that is the poly-Si contact and the c-Si top surface. Moreover, as the ToF-SIMS sputtering time was not converted into thickness (as explained in **section 2.2**), the O profiles were used to detect the interfacial SiO_x layer, which is located at a sputtering time of 520 s and 570 s for poly-Si(i) and poly-Si(B) contacts, respectively.
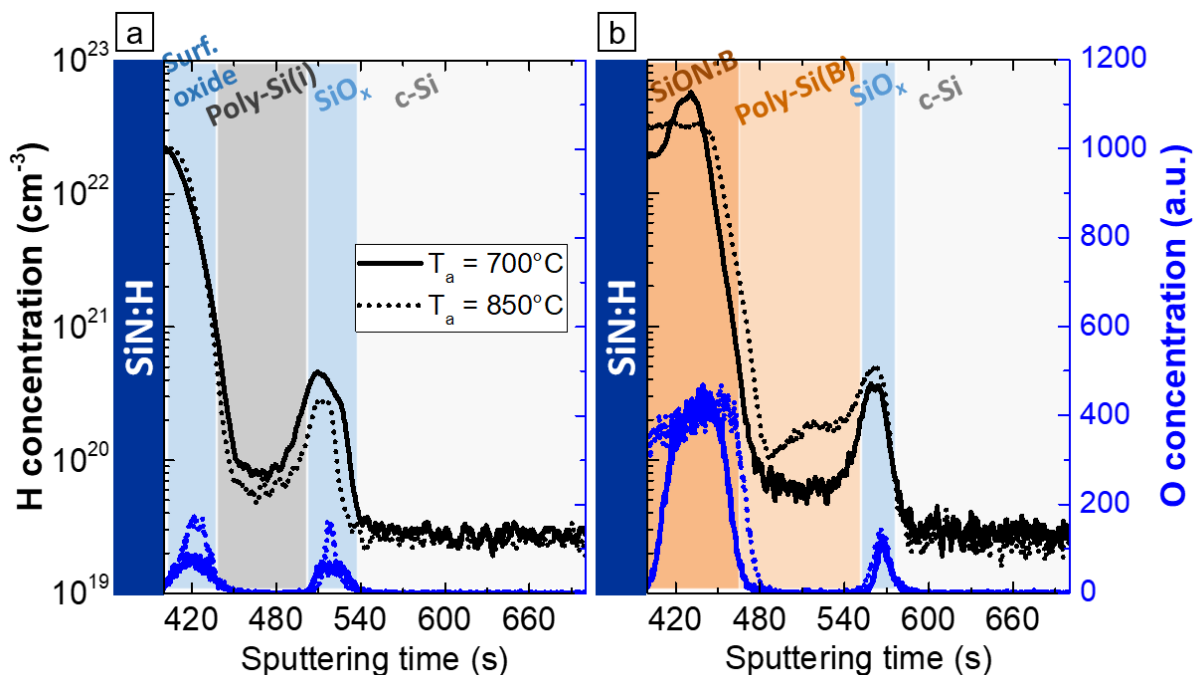
Figure 7. H and O concentration profiles (represented by black and blue lines, respectively) as measured by ToF-SIMS on samples featuring the poly-Si(i)/SiO_x (a) and the poly-Si(B)/SiO_x (b) contacts. Measurements were performed after SiN:H deposition on samples annealed at T_a = 700 °C (solid curves) and 850 °C (dashed curves).

Firstly, focusing on H concentration profiles (black lines in **Figure 7**), one can observe for both poly-Si(i) and poly-Si(B) contacts:

- An accumulation of H at a sputtering time of 420 s, i.e. in an oxide layer detected at the poly-Si top surface and in the SiON:B layer for poly-Si(i) and poly-Si(B) contacts, respectively;

- An accumulation of H at the interfacial SiO_x layer with a similar concentration of approximately 3×10^{20} cm^{-3} for all the investigated samples.

Regarding the former observation, the H accumulation detected in the surface oxide and SiON:B layers for poly-Si(i) and poly-Si(B) samples, respectively, could be due to the presence of the SiN:H layer on top of these layers coupled to their amorphous nature that offers available bonding sites for H atoms.

The latter observation confirms that H atoms diffused from the SiN:H layer to the interfacial SiO_x layer, likely providing further chemical passivation of the interface between the poly-Si contact and the c-Si substrate. This result is in good agreement with results recently reported by other groups [35–37]. We note that, in the frame of this study, the H concentration profile was also measured on a monitoring sample before SiN:H deposition and no accumulation of H was observed at the interface (not shown here). The similar H concentration profiles measured in the interfacial SiO_x layer for all the investigated samples disproves the hypothesis that the decreasing iV_{oc} gain with increasing T_a after hydrogenation would result from a lower accumulation of H at the interface. A different bonding structure of H at the interface and/or structure of the interface could rather explain the different surface passivation properties observed in **section 3.1**. We note nonetheless that the similar H concentration observed in the region of the interfacial SiO_x layer for both doped and intrinsic contacts emphasizes that the SiON:B doping layer did not impede the diffusion of H towards this interface. Overall, the only significant difference we could observe between the different H profiles measured here was a higher H concentration in the poly-Si(B) layer after annealing at $T_a = 850\,°C$. This result may indicate a higher concentration of defects passivated by H in this layer, that could be B- and/or O-related [9].

Now focusing on O concentration profiles (blue lines in **Figure 7**), one can observe that for both poly-Si(i) and poly-Si(B) contacts a peak of O was measured at the poly-Si top

surface. For poly-Si(i) contacts, this O signal likely results from the oxidation of the poly-Si(i) layer's surface, that may have intensified during annealing of the layer due to high-temperature and a potential residual O concentration in the tube furnace. For poly-Si(B) contacts, the high and large O signal detected at the poly-Si surface corresponds to the SiON:B doping layer. As mentioned, the O concentration profiles were used to locate the interfacial SiO_x layer, which was detected at a sputtering time of 520 s and 570 s for poly-Si(i) and poly-Si(B) contacts, respectively. One can observe that, for $T_a = 700\,°C$, the O peak related to the SiO_x layer appeared more intense and better defined for the B-doped poly-Si contact than for its intrinsic counterpart. This observation could result from the diffusion of O atoms from the SiON:B layer to the interface during annealing, resulting in a O-richer SiO_x layer for the poly-Si(B) contact, as already suggested by EELS analyses (see **Figure 5**). For poly-Si(i) contacts, the modification of both O peaks shape toward thinner and better defined peaks observed with increasing T_a from 700 °C to 850 °C could result from a reorganization of these interfaces at higher T_a but would require further investigations to be fully understood.

3.3. Comprehensive understanding of the passivation scheme

In this last section, we propose a comprehensive understanding of the mechanisms that yield the passivation of the interface of our ex-situ doped poly-Si contact based on the different results presented above.

We first discuss the passivation scheme after annealing for dopant diffusion, which is schematically depicted in **Figure 8**. In **section 3.1**, we compared the iV_{oc} values obtained with intrinsic and highly-doped poly-Si/SiO_x contacts at different steps of the fabrication process. After annealing, we obtained decent iV_{oc} values only with the doped contact that also demonstrated a better stability with increasing T_a. This allows us to conclude that, at this stage of the process, the surface passivation is mostly ensured by field-effect passivation. Moreover, for the doped contact, we observed:

- By means of ECV analyses (presented in **section 3.2.2**), a gradual diffusion of active B dopants in the poly-Si layer and at the c-Si surface with increasing T_a, which likely explains the increase of iV_{oc} with increasing T_a observed after annealing;

- By means of EELS and ToF-SIMS analyses (presented in **sections 3.2.1** and **3.2.3**, respectively), a higher concentration of O in the interfacial SiO_x layer compared to

the intrinsic contact. This suggests a diffusion of O from the SiON:B layer to the SiO_x interface during annealing, and could (at least partly) explain the better stability of passivation with increasing T_a observed for the doped contact.

For the intrinsic contact, the slight decrease of iV_{oc} observed for T_a = 850 °C could result from modifications experienced by the thin SiO_x layer during annealing, e.g. a degradation of its homogeneity along the interface at high T_a.

The passivation scheme after hydrogenation performed subsequently to the annealing step is depicted in **Figure 9**. After hydrogenation, both intrinsic and doped contacts demonstrated an increase of iV_{oc} on all the investigated T_a range. This increase was more pronounced for the intrinsic contact than for the B-doped one. It was also more pronounced at low annealing temperature. Thus, for T_a = 700 °C, we observed an increase of iV_{oc} of 100 and 200 mV for B-doped and intrinsic contacts, respectively, while for T_a = 850°C the increase was only of 15 and 57 mV. These results indicate that, after hydrogenation, the chemical passivation of the interface, ensured by the thin SiO_x layer and the accumulation of H, becomes of first importance. Therefore, at this stage of the process, it appears important to have preserved the homogeneity of the SiO_x layer which allows for H accumulation [35]. The investigation of H concentration profiles by ToF-SIMS presented in **section 3.2.3** confirmed the accumulation of H in the interfacial SiO_x layer, but did not allow us to observe a clear difference of H concentration at the interface of samples annealed at low and high T_a.
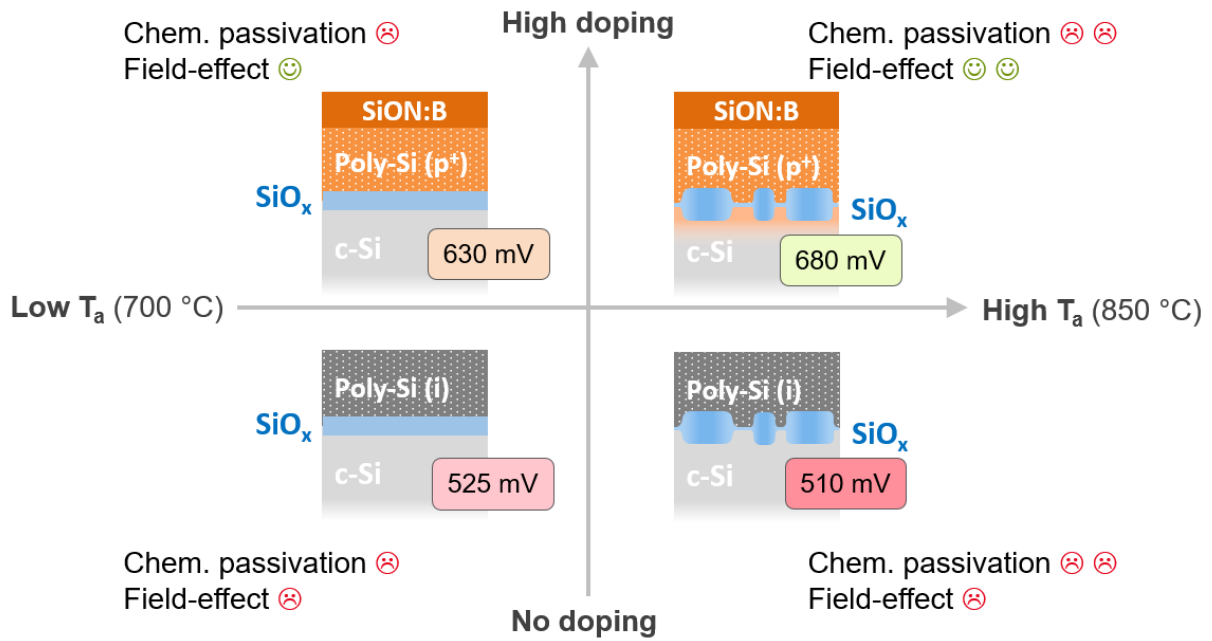
Figure 8. Schematic picture summarizing the respective effects of chemical and field-effect passivation of B-doped (top) and intrinsic (bottom) samples after the annealing step used for crystallization and doping of the poly-Si layer, as a function of the annealing temperature (T_a). For the sake of simplicity, only the extreme T_a of the range investigated in this work are represented (i.e. 700 °C and 850 °C) with corresponding iV_{oc} values.
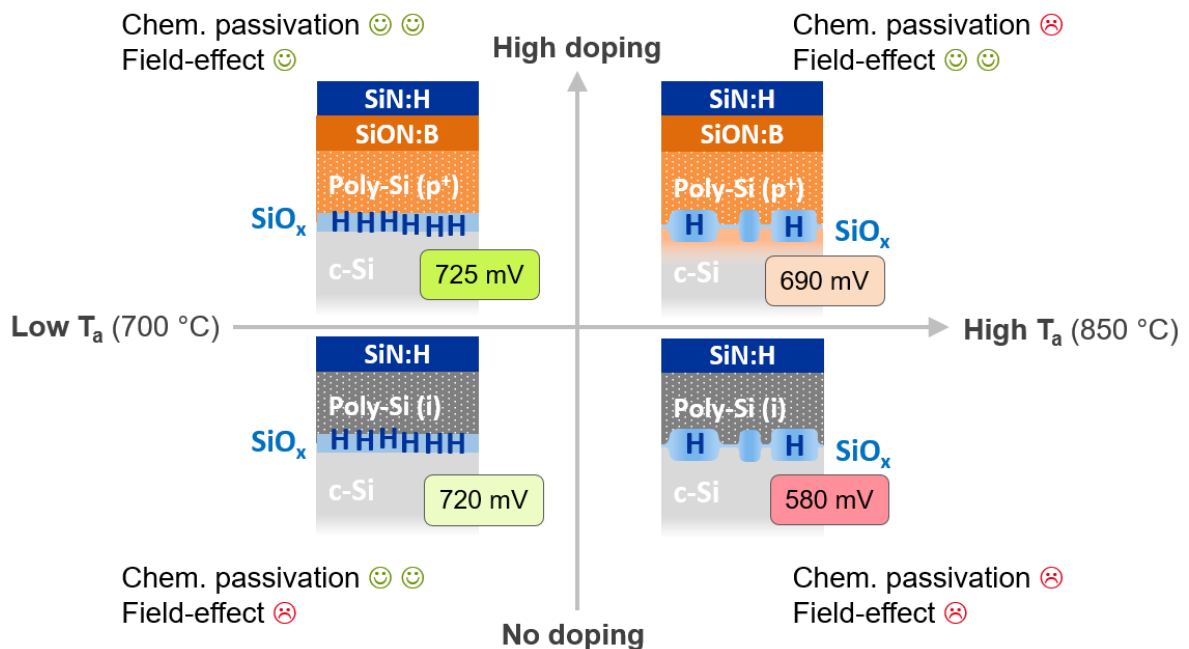
Figure 9. Schematic picture summarizing the respective effects of chemical and field-effect passivation of B-doped (top) and intrinsic (bottom) samples after subsequent hydrogenation and firing steps as a function of the annealing temperature (T_a). For the sake of simplicity, only the

extreme T_a of the range investigated in this work are represented (i.e. 700 °C and 850 °C) with corresponding iV_{oc} values.

4. Conclusion

In this work, we reported on a hole-selective poly-Si/SiO$_x$ passivating contact fabricated by depositing an intrinsic Si layer (denoted 'as-dep Si(i)') on top of a thin SiO$_x$ layer, followed by ex-situ doping of the as-dep Si(i) layer through the deposition of a B-rich dielectric layer (SiON:B) and an annealing step at high temperature (T_a = 700-850 °C). We took advantage of this ex-situ doping process to investigate the respective contributions of the chemical passivation (provided by the thin SiO$_x$ layer and additional H diffusion) and the field-effect passivation (provided by the high-doping of the poly-Si layer). Our results suggest a change of the passivation regime during the fabrication process of the ex-situ doped poly-Si/SiO$_x$ contact: after annealing, the surface passivation is mostly ensured by field-effect passivation whereas after hydrogenation the chemical passivation of the interface through a homogeneous SiO$_x$ layer that allows for H accumulation becomes of first importance.

To get further insights into the passivation scheme of our ex-situ doped poly-Si contact, we performed further analyses by means of STEM, EELS, ECV and ToF-SIMS measurements. We observed the stability of the as-dep Si(i) layer's microstructure both after annealing at high temperature (T_a = 800 °C) and after ex-situ doping. We then investigated the doping profile obtained by ex-situ doping as a function of the annealing temperature (T_a) and observed a gradual doping of the poly-Si layer with increasing T_a, which strengthens the field-effect passivation. We also observed a higher O concentration in the interfacial SiO$_x$ layer of the doped contact compared to its intrinsic counterpart, resulting from the diffusion of O from the SiON:B doping layer during annealing and likely explaining the better stability of passivation with increasing T_a of the doped contact. Finally, we investigated the H concentration profile in both intrinsic and doped poly-Si/SiO$_x$ contacts and observed an accumulation of H in the interfacial SiO$_x$ layer, confirming that the diffusion of H in the samples provides a further chemical passivation of this interface.

The surface passivation properties obtained with the ex-situ doped poly-Si/SiO$_x$ contact (iV_{oc} = 733 mV and J_0 = 6.1 fA.cm^{-2}) are very promising for the following integration of this contact in a device (e.g. at the rear side of a p-type c-Si solar cell) [12,15,36,38]. However,

these best surface passivation properties were demonstrated with poly-Si(B) contacts annealed at T_a = 700 °C that feature a very shallow B diffusion in the c-Si and thus a high resistivity. Therefore, our efforts are currently focused on finding a compromise between high surface passivation properties and low resistivity of the poly-Si(B) passivating stack to achieve a successful integration of this contact in a device.

Funding

Acknowledgements

References

[1] S.W. Glunz, F. Feldmann, A. Richter, M. Bivour, C. Reichel, H. Steinkemper, J. Benick, M. Hermle, The irresistible charm of a simple current flow pattern - 25% with a solar cell featuring a full-area back contact, Proc. 31st Eur. Photovolt. Sol. Energy Conf. Exhib. (2015) Hamburg, Germany.

[2] Y. Chen, H. Shen, P.P. Altermatt, Analysis of recombination losses in screen-printed aluminum-alloyed back surface fields of silicon solar cells by numerical device simulation, Sol. Energy Mater. Sol. Cells. 120 (2014) 356–362. https://doi.org/10.1016/j.solmat.2013.05.051.

[3] A. Richter, J. Benick, F. Feldmann, A. Fell, M. Hermle, S.W. Glunz, n-Type Si solar cells with passivating electron contact: Identifying sources for efficiency limitations by wafer thickness and resistivity variation, Sol. Energy Mater. Sol. Cells. 173 (2017) 96–105. https://doi.org/10.1016/j.solmat.2017.05.042.

[4] F. Haase, C. Hollemann, S. Schäfer, A. Merkle, M. Rienäcker, J. Krügener, R. Brendel, R. Peibst, Laser contact openings for local poly-Si-metal contacts enabling 26.1%-efficient POLO-IBC solar cells, Sol. Energy Mater. Sol. Cells. 186 (2018) 184–193. https://doi.org/10.1016/j.solmat.2018.06.020.

[5] Y. Chen, D. Chen, C. Liu, Z. Wang, Y. Zou, Y. He, Y. Wang, L. Yuan, J. Gong, W. Lin, X. Zhang, Y. Yang, H. Shen, Z. Feng, P.P. Altermatt, P.J. Verlinden, Mass production of industrial tunnel oxide passivated contacts (i-TOPCon) silicon solar cells with average efficiency over 23% and modules over 345 W, Prog. Photovolt. Res. Appl. 27 (2019) 827–834. https://doi.org/10.1002/pip.3180.

[6]   D. Chen, Y. Chen, Z. Wang, J. Gong, C. Liu, Y. Zou, Y. He, Y. Wang, L. Yuan, W. Lin, R. Xia, L. Yin, X. Zhang, G. Xu, Y. Yang, H. Shen, Z. Feng, P.P. Altermatt, P.J. Verlinden, 24.58% total area efficiency of screen-printed, large area industrial silicon solar cells with the tunnel oxide passivated contacts (i-TOPCon) design, Sol. Energy Mater. Sol. Cells. 206 (2020) 110258. https://doi.org/10.1016/j.solmat.2019.110258.

[7]   J. Stuckelberger, G. Nogay, P. Wyss, Q. Jeangros, C. Allebé, F. Debrot, X. Niquille, M. Ledinsky, A. Fejfar, M. Despeisse, F.-J. Haug, P. Löper, C. Ballif, Passivating electron contact based on highly crystalline nanostructured silicon oxide layers for silicon solar cells, Sol. Energy Mater. Sol. Cells. 158 (2016) 2–10. https://doi.org/10.1016/j.solmat.2016.06.040.

[8]   G. Nogay, J. Stuckelberger, P. Wyss, E. Rucavado, C. Allebé, T. Koida, M. Morales-Masis, M. Despeisse, F.-J. Haug, P. Löper, C. Ballif, Interplay of annealing temperature and doping in hole selective rear contacts based on silicon-rich silicon-carbide thin films, Sol. Energy Mater. Sol. Cells. 173 (2017) 18–24. https://doi.org/10.1016/j.solmat.2017.06.039.

[9]   B. Nemeth, D.L. Young, M.R. Page, V. LaSalvia, S. Johnston, R. Reedy, P. Stradins, Polycrystalline silicon passivated tunneling contacts for high efficiency silicon solar cells, J. Mater. Res. 31 (2016) 671–681. https://doi.org/10.1557/jmr.2016.77.

[10]   Y. Tao, V. Upadhyaya, Y.-Y. Huang, C.-W. Chen, K. Jones, A. Rohatgi, Carrier selective tunnel oxide passivated contact enabling 21.4% efficient large-area n-type silicon solar cells, in: Photovolt. Spec. Conf. PVSC 2016 IEEE 43rd, IEEE, 2016: pp. 2531–2535.

[11]   A. Morisset, R. Cabal, B. Grange, C. Marchat, J. Alvarez, M.-E. Gueunier-Farret, S. Dubois, J.-P. Kleider, Highly passivating and blister-free hole selective poly-silicon based contact for large area crystalline silicon solar cells, Sol. Energy Mater. Sol. Cells. 200 (2019) 109912. https://doi.org/10.1016/j.solmat.2019.109912.

[12]   G. Nogay, A. Ingenito, E. Rucavado, Q. Jeangros, J. Stuckelberger, P. Wyss, M. Morales-Masis, F.-J. Haug, P. Loper, C. Ballif, Crystalline Silicon Solar Cells With Coannealed Electron- and Hole-Selective SiC $_\text{x}$ Passivating Contacts, IEEE J. Photovolt. (2018) 1–8. https://doi.org/10.1109/JPHOTOV.2018.2866189.

[13]   A. Cuevas, Y. Wan, D. Yan, C. Samundsett, T. Allen, X. Zhang, J. Cui, J. Bullock, Carrier population control and surface passivation in solar cells, Sol. Energy Mater. Sol. Cells. 184 (2018) 38–47. https://doi.org/10.1016/j.solmat.2018.04.026.

[14]   S.W. Glunz, M. Bivour, C. Messmer, F. Feldmann, R. Müller, C. Reichel, A. Richter, F. Schindler, J. Benick, M. Hermle, Passivating and carrier-selective contacts—Basic requirements and implementation, in: 44th IEEE Photovolt. Spec. Conf. PVSC, 2017.

[15]   S. Mack, J. Schube, T. Fellmeth, F. Feldmann, M. Lenes, J.-M. Luchies, Metallisation of Boron-Doped Polysilicon Layers by Screen Printed Silver Pastes, Phys. Status Solidi RRL - Rapid Res. Lett. 11 (2017) 1700334. https://doi.org/10.1002/pssr.201700334.

[16]   R. van der Vossen, F. Feldmann, A. Moldovan, M. Hermle, Comparative study of differently grown tunnel oxides for -type passivating contacts, in: Energy Procedia, 2017: pp. 448–454.

[17]   A.S. Kale, W. Nemeth, S.P. Harvey, M. Page, D.L. Young, S. Agarwal, P. Stradins, Effect of silicon oxide thickness on polysilicon based passivated contacts for high-efficiency crystalline silicon solar cells, Sol. Energy Mater. Sol. Cells. 185 (2018) 270–276. https://doi.org/10.1016/j.solmat.2018.05.011.

[18] A. Morisset, R. Cabal, V. Giglia, B. Grange, J. Alvarez, M.-E. Gueunier-Farret, S. Dubois, J.-P. Kleider, SiOxNy:B layers for ex-situ doping of hole-selective poly silicon contacts: A passivation study, in: 2019: p. 040012. https://doi.org/10.1063/1.5123839.

[19] G.E. Jellison, M.F. Chisholm, S.M. Gorbatkin, Optical functions of chemical vapor deposited thin-film silicon determined by spectroscopic ellipsometry, Appl. Phys. Lett. 62 (1993) 3348–3350. https://doi.org/10.1063/1.109067.

[20] D.E. Aspnes, A.A. Studna, E. Kinsbron, Dielectric properties of heavily doped crystalline and amorphous silicon from 1.5 to 6.0 eV, Phys. Rev. B. 29 (1984) 768.

[21] D.E. Kane, R.M. Swanson, Measurement of the emitter saturation current by a contactless photoconductivity decay method (silicon solar cells), Conf. Rec. IEEE Photovolt. Spec. Conf. (1985) 578–583.

[22] D.L. Young, W. Nemeth, V. LaSalvia, R. Reedy, N. Bateman, P. Stradins, Ion implanted passivated contacts for interdigitated back contacted solar cells, in: 2015 IEEE 42nd Photovolt. Spec. Conf. PVSC, IEEE, New Orleans, LA, 2015: pp. 1–5. https://doi.org/10.1109/PVSC.2015.7356141.

[23] W. Liu, X. Yang, J. Kang, S. Li, L. Xu, S. Zhang, H. Xu, J. Peng, F. Xie, J.-H. Fu, K. Wang, J. Liu, A. Alzahrani, S. De Wolf, Polysilicon Passivating Contacts for Silicon Solar Cells: Interface Passivation and Carrier Transport Mechanism, ACS Appl. Energy Mater. 2 (2019) 4609–4617. https://doi.org/10.1021/acsaem.8b02149.

[24] J.-I. Polzin, F. Feldmann, B. Steinhauser, M. Hermle, S.W. Glunz, Study on the interfacial oxide in passivating contacts, in: AIP Conf Proc 2147, Leuven, Belgium, 2019: p. 040016. https://doi.org/10.1063/1.5123843.

[25] G. Yang, A. Ingenito, O. Isabella, M. Zeman, IBC c-Si solar cells based on ion-implanted poly-silicon passivating contacts, Sol. Energy Mater. Sol. Cells. 158 (2016) 84–90. https://doi.org/10.1016/j.solmat.2016.05.041.

[26] K.R. McIntosh, P.P. Altermatt, A freeware 1D emitter model for silicon solar cells, in: 2010 35th IEEE Photovolt. Spec. Conf., IEEE, Honolulu, HI, USA, 2010: pp. 002188–002193. https://doi.org/10.1109/PVSC.2010.5616124.

[27] J. Stuckelberger, P. Loper, C. Ballif, G. Nogay, P. Wyss, A. Ingenito, C. Allebe, J. Horzel, B.A. Kamino, M. Despeisse, F.-J. Haug, Recombination Analysis of Phosphorus-Doped Nanostructured Silicon Oxide Passivating Electron Contacts for Silicon Solar Cells, IEEE J. Photovolt. 8 (2018) 389–396. https://doi.org/10.1109/JPHOTOV.2017.2779871.

[28] S. Li, M. Pomaska, J. Hoß, J. Lossen, M. Ziegner, R. Hong, F. Finger, U. Rau, K. Ding, In Situ-Doped Silicon Thin Films for Passivating Contacts by Hot-Wire Chemical Vapor Deposition with a High Deposition Rate of 42 nm/min, ACS Appl. Mater. Interfaces. 11 (2019) 30493–30499. https://doi.org/10.1021/acsami.9b10360.

[29] J. Schmidt, A.G. Aberle, Carrier recombination at silicon–silicon nitride interfaces fabricated by plasma-enhanced chemical vapor deposition, J. Appl. Phys. 85 (1999) 3626–3633. https://doi.org/10.1063/1.369725.

[30] J. Koh, Y. Lee, H. Fujiwara, C.R. Wronski, R.W. Collins, Optimization of hydrogenated amorphous silicon p-i-n solar cells with two-step i layers guided by real-time spectroscopic ellipsometry, Appl. Phys. Lett. 73 (1998) 1526.

[31] P. Wyss, J. Stuckelberger, G. Nogay, J. Horzel, Q. Jeangros, I. Mack, M. Lehmann, X. Niquille, C. Allebe, M. Despeisse, F.-J. Haug, A. Ingenito, P. Loper, C. Ballif, A Mixed-Phase SiO$_x$ Hole Selective Junction Compatible With High Temperatures Used in Industrial Solar Cell Manufacturing, IEEE J. Photovolt. 10 (2020) 1262–1269. https://doi.org/10.1109/JPHOTOV.2020.3006979.

[32] F. Feldmann, J. Schön, J. Niess, W. Lerch, M. Hermle, Studying dopant diffusion from Poly-Si passivating contacts, Sol. Energy Mater. Sol. Cells. 200 (2019) 109978. https://doi.org/10.1016/j.solmat.2019.109978.

[33] R. Bock, P.P. Altermatt, J. Schmidt, Accurate extraction of doping profiles from electrochemical capacitance voltage measurements, Proc 23rd Eur Photovolt Sol Energy Conf Exhib. Valencia, Spain (2008) 1510–1513.

[34] R. Cabal, T. Blévin, R. Monna, Y. Veschetti, S. Dubois, Multifunctional Dielectric Layers for the Fabrication of Ultra-Simplified n-PERT c-Si Solar Cells, Energy Procedia. 92 (2016) 684–690. https://doi.org/10.1016/j.egypro.2016.07.044.

[35] M. Lehmann, N. Valle, J. Horzel, A. Pshenova, P. Wyss, M. Döbeli, M. Despeisse, S. Eswara, T. Wirtz, Q. Jeangros, A. Hessler-Wyser, F.-J. Haug, A. Ingenito, C. Ballif, Analysis of hydrogen distribution and migration in fired passivating contacts (FPC), Sol. Energy Mater. Sol. Cells. 200 (2019) 110018. https://doi.org/10.1016/j.solmat.2019.110018.

[36] D.L. Young, B.G. Lee, D. Fogel, W. Nemeth, V. LaSalvia, S. Theingi, M. Page, M. Young, C. Perkins, P. Stradins, Gallium-Doped Poly-Si:Ga/SiO2 Passivated Emitters to n-Cz Wafers With iV oc >730 mV, IEEE J. Photovolt. 7 (2017) 1640–1645. https://doi.org/10.1109/JPHOTOV.2017.2748422.

[37] M. Schnabel, B.W.H. van de Loo, W. Nemeth, B. Macco, P. Stradins, W.M.M. Kessels, D.L. Young, Hydrogen passivation of poly-Si/SiO$_x$ contacts for Si solar cells using Al$_2$O$_3$ studied with deuterium, Appl. Phys. Lett. 112 (2018) 203901. https://doi.org/10.1063/1.5031118.

[38] D. Yan, A. Cuevas, S.P. Phang, Y. Wan, D. Macdonald, 23% efficient p-type crystalline silicon solar cells with hole-selective passivating contacts based on physical vapor deposition of doped silicon films, Appl. Phys. Lett. 113 (2018) 061603. https://doi.org/10.1063/1.5037610.